FULL PAPER

Solar Cells

ADVANCED
ENERGY
MATERIALS

www.advenergymat.de

Anomalous Charge-Extraction Behavior for Graphene-Oxide (GO) and Reduced Graphene-Oxide (rGO) Films as Efficient p-Contact Layers for High-Performance Perovskite Solar Cells

Efat Jokar, Zhong Yi Huang, Sudhakar Narra, Chi-Yung Wang, Vidya Kattoor, Chih-Chun Chung, and Eric Wei-Guang Diau*

Reduced graphene oxides (rGO) are synthesized via reduction of GO with reducing agents as a hole-extraction layer for high-performance inverted planar heterojunction perovskite solar cells. The best efficiencies of power conversion (PCE) of these rGO cells exceed 16%, much greater than those made of GO and poly(3,4-ethenedioxythiophene):poly(styrenesulfonate) films. A flexible rGO device shows PCE 13.8% and maintains 70% of its initial performance over 150 bending cycles. It is found that the hole-extraction period is much smaller for the GO/methylammonium lead-iodide perovskite (PSK) film than for the other rGO/PSK films, which contradicts their device performances. Photoluminescence and transient photoelectric decays are measured and control experiments are performed to prove that the reduction of the oxygen-containing groups in GO significantly decreases the ability of hole extraction from PSK to rGO and also retards the charge recombination at the rGO/PSK interface. When the hole injection from PSK to GO occurs rapidly, hole propagation from GO to the indium-doped tin oxide (ITO) substrate becomes a bottleneck to overcome, which leads to a rapid charge recombination that decreases the performance of the GO device relative to the rGO device.

1. Introduction

Hybrid lead-halide perovskite solar cells (PSC) have achieved a greatly enhanced performance of conversion of solar energy, with reported efficiencies approaching those of crystalline-silicon solar cells.[1] Methylammonium lead-iodide perovskite ($CH_3NH_3PbI_3$, abbreviated as PSK hereafter), as semiconducting pigment with direct band gap 1.55 eV, which shows excellent light-harvesting and ambipolar charge transport, has been applied in high-performance perovskite solar cells.[2] Based on this ambipolar charge-transport property and a la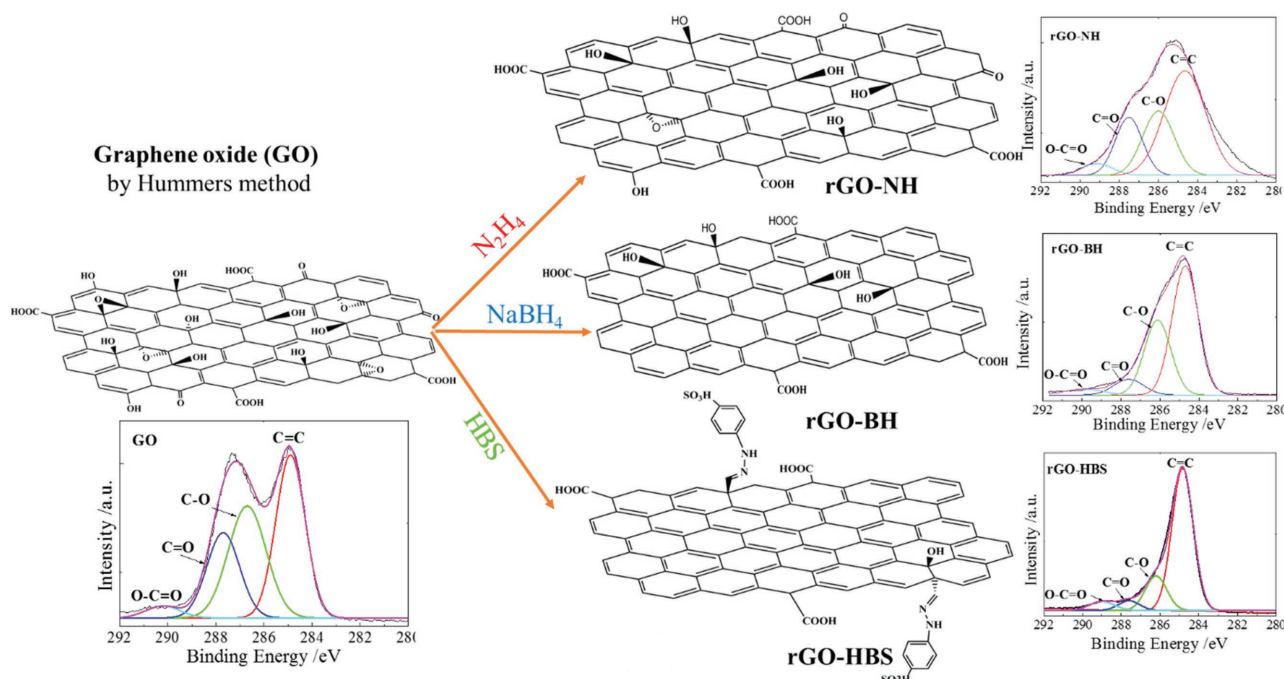rge diffusion length for electrons and holes in a perovskite structure, thin-film perovskite solar cells with a planner heterojunction (PHJ) configuration were introduced.[2c,3] In the PHJ structure, the perovskite layer serves as a light absorber between the two electrodes to transport electron and hole carriers. The PHJ device hence avoids the problem of pore filling in regular mesoscopic PSC and simplifies the device fabrication with satisfactory device performance.[4] Moreover, the PHJ cell can be fabricated at temperatures < 150 °C with solution-based methods; this advantage is promising for the development of flexible perovskite solar cells.[5] PHJ devices of two types have been reported with either a regular (n–i–p type) or an inverted (p–i–n) configuration.[3,6] Various materials have been used as the hole-extraction or electron-extraction layer (HEL or EEL) in these configurations.[6b,7] Various organic and inorganic hole-transport materials have been reported for inverted PHJ PSC.[3,8]

A suitable HEL material should have primary requirements such as (i) effective hole mobility, (ii) a compatible HOMO (or valence-band) energy level relative to perovskite, (iii) sufficient solubility and film-formation properties, (iv) great transparency in the visible region, and (v) modest cost.[3] The most common HEL reported for inverted PSC is poly(3,4-ethenedioxythiophene):poly(styrenesulfonate) (PEDOT:PSS). Although PEDOT-based PHJ solar cells have been reported to have great efficiency,[9] problems of PEDOT:PSS such as electrical inhomogeneity, great acidity and hygroscopic properties cause them to exhibit poor long-term stability.[10] Inorganic hole-transport materials such as NiO_x,[10b,11] V_2O_5,[12] MoO_3,[13] CoO_x,[20] and many others[14] were introduced to replace PEDOT:PSS for their satisfactory stability, but fabrication of these inorganic HEL requires expensive vacuum or high-temperature processing.

As a robust HEL alternative, PSC made of graphene oxide (GO) have been reported by Wu et al.[15a] and Chung et al.[15b] to deliver an efficiency of power conversion (PCE) over 12%. Although graphene oxide has unique optical and electronic properties, its insulator property limits its application as HEL for PSC.[16] Reduction of GO (rGO) is an effective route

Dr. E. Jokar, Z. Y. Huang, Dr. S. Narra, C.-Y. Wang, V. Kattoor,
C.-C. Chung, Prof. E. W.-G. Diau
Department of Applied Chemistry and Institute of Molecular Science
National Chiao Tung University
No. 1001, Ta-Hsueh Rd, Hsinchu 30010, Taiwan
E-mail: diau@mail.nctu.edu.tw

1701640 (1 of 10)

**ADVANCED
SCIENCE NEWS**
www.advancedsciencenews.com

**ADVANCED
ENERGY
MATERIALS**
www.advenergymat.de

Scheme 1. Schematic representation of reduction of graphene oxide (GO) with various reducing agents as indicated; their corresponding XPS spectra are shown.

to improve the conductivity of the GO nanosheets. Yeo et al. reported the first rGO-based PHJ inverted PSC with PCE 10.8%.[17] In their work, a GO-based device attained PCE only 4.0%, which is much less than that reported by Wu et al.[15] The conductivity, hydrophilicity, and surface chemistry of rGO nanosheets depend on the reduction procedure such as the type of reducing agent, proportion of reducing agent, and the reaction conditions.[18] Even though GO and rGO are promising HEL for PHJ PSC devices, the published results[15,17,19] are therefore controversial; systematic investigations of those materials are required to understand their optoelectronic properties and to optimize their photovoltaic performances.

Here we report our detailed results on the characterization of GO and rGO nanosheets deposited on an In-doped SnO_2 (ITO) substrate as HEL for inverted PHJ PSC. According to the schematic diagram in **Scheme 1**, GO made with the Hummers method (Figures S1, Supporting Information) was reduced with three reagents, hydrazine (N_2H_4), sodium borohydride ($NaBH_4$), and 4-hydrazino benzenesulfonic acid, to produce three rGO, labeled rGO-NH, rGO-BH, and rGO-4-hydrazino benzenesulfonic acid (HBS), respectively; the corresponding X-ray photoelectron spectra (XPS) spectra shown in Scheme 1 demonstrate the varied extent of reduction of those rGO. PEDOT:PSS served as HEL for comparison. The device efficiencies exhibited an order rGO-HBS > rGO-NH > rGO-BH > PEDOT:PSS > GO, for which both rGO-HBS and rGO-NH devices showed the best PCE, exceeding 16%. We recorded photoluminescence (PL) spectra, transient PL decays and transient photovoltage decays; these results show that GO is an efficient hole-extraction layer to quench PL more effectively than the other rGO, but the photocurrents and the fill factors of the GO devices were much smaller than those of the other

rGO devices. The control experiments showed that both the PL intensity and the lifetime of GO were enhanced when the oxygen-containing functional groups on the surface of GO were reduced with hydrazine vapor at 50 and 100 °C. We expect that holes were efficiently extracted from perovskite to GO but also trapped on the surface of GO on the localized oxygen atoms that might facilitate electron–hole recombination at the PSK/GO interface. Once those oxygen-containing groups (such as −C−O−C−, −C−OH, and −C−COOH) are reduced appropriately, the delocalized holes on the graphene ring can transport freely to the ITO substrate so that photocurrents became larger in the rGO device than in the GO device. The effect of the reducing level of GO on the ITO surface coverage was recognized to affect the PV performance of the rGO device. Flexible devices were fabricated for rGO deposited on the ITO/polyethylene 2,6-naphthalate (PEN) substrate; the rGO-NH device showed PCE 13.8% and retained 70% of the original device performance after continuous bending for more than 150 cycles.

2. Results and Discussion

A graphene oxide monolayer was synthesized with the Hummers method (Figure S1, Supporting Information).[20] The chemical compositions of the obtained GO and rGO samples were examined with XPS (Scheme 1), Raman and infrared spectra (Figure S2a,b, Supporting Information, respectively). The characteristic G line in the Raman spectrum corresponding to the first-order scattering of the E_{2g} phonon of the trigonal carbon atoms with sp² character in GO was observed at 1605 cm⁻¹; this line was slightly shifted to 1600 and 1601 cm⁻¹ for rGO-NH and rGO-BH, respectively. The red shift

**ADVANCED
SCIENCE NEWS**
www.advancedsciencenews.com

**ADVANCED
ENERGY
MATERIALS**
www.advenergymat.de

of the G line is related to removal of oxygen groups on reduction of GO.[21] This reduction is confirmed by the infrared spectra (Figure S2b, Supporting Information) and XPS (Scheme 1 and Table S1, Supporting Information). Oxygen-containing functional groups of three types were deduced from the infrared spectra, O−H stretching mode at 3400 cm^{-1}, C=O stretching mode at 1720 cm^{-1}, C=C stretching mode at 1600 cm^{-1}, C−OH stretching mode at 1220 cm^{-1}, and C−O stretching mode at 1060 cm^{-1}.[22] The intensities of infrared absorption of the C−O and C=O functional groups decreased upon reduction of GO into rGO-NH and rGO-BH. For rGO-HBS, although the G line in the Raman spectrum of rGO-HBS became shifted to 1611 cm^{-1}, this feature is attributed to the existence of sulfonic acid groups on the graphene nanosheets that would induce a negative dipole moment oriented out of the plane of the graphene surface (Scheme 1). This negative dipolar moment causes a stable aqueous suspension and might generate a uniform


Figure 1. SEM images of thin films of a) GO, b) rGO-NH, c) rGO-BH, and d) rGO-HBS deposited on the surface of ITO as hole-extraction layer in perovskite solar cells. The small light gray area in each image represents the uncovered ITO surface.

film with satisfactory conductivity.[23] The presence of the SO_3 group in the rGO-HBS film is illustrated in infrared spectra with vibrational modes observed at 1187, 1130, and 1008 cm^{-1} corresponding to S=O stretching, S−O stretching, and C−H bending motions, respectively.[24] Further details about the extent of reduction of GO sheets were deduced from XPS of the C1s core level; the characteristic XPS signals shown in Scheme 1 were deconvoluted into four components, which are attributed to the trigonally coordinated carbons in C=C, C−O, C=O, and O−C=O groups, respectively. The fraction of carbon bonds of various types was determined with the deconvoluted XPS spectra, as shown in Table S1 (Supporting Information). The proportion of C=C bonds increased on reduction of GO with these reducing agents, with mild reduction by hydrazine and $NaBH_4$, but for rGO-HBS most oxygen-containing functional groups were reduced with HBS.

Figure 1 shows scanning electron micrographs (SEM) images for GO and rGO films deposited on the ITO substrate; the corresponding AFM images on a Si substrate appear in Figure S3 (Supporting Information). The GO film (Figure 1a and Figure S3a, Supporting Information) exhibits a nanosheet feature with 1–3 layers; the thickness is estimated to be ≈ 2–3 nm, similar to what has been reported.[16c] On reduction of graphene oxide, the number of oxygen-containing groups decreased and the nanosheets of rGO had less interaction with the ITO surface than the GO nanosheet.[25] During the spin coating, most rGO nanosheets thus spread from the ITO surface, leaving a film slightly thinner than that of GO for both rGO-NH (Figure 1b and Figure S3b, Supporting Information) and rGO-HBS (Figure 1d and Figure S3d, Supporting Information) films. For the rGO-BH film (Figure 1c and Figure S3c, Supporting Information), the surface coverage seemed to be poorer than for other samples because of aggregation of the rGO-BH nanosheets. rGO-NH had a mild
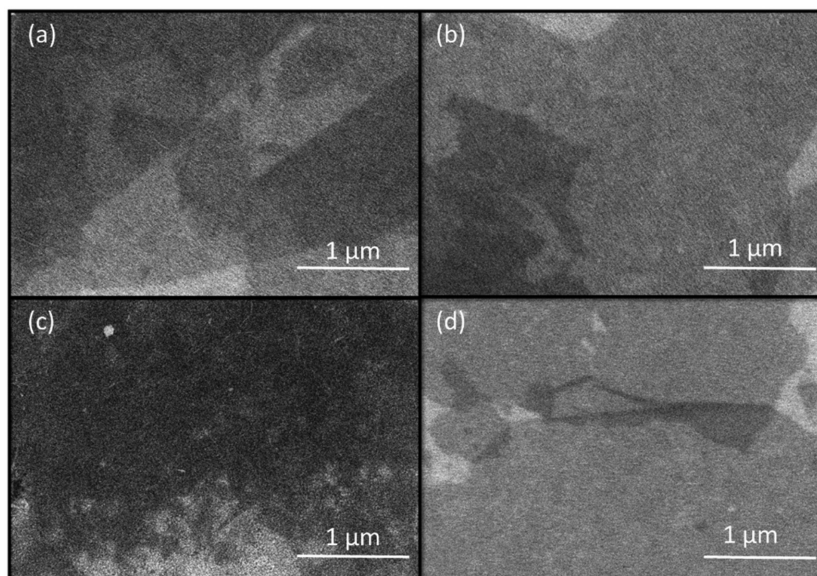
reduction but rGO-HBS had a strong reduction as the graphene surface was functionalized with the hydrophilic SO_3H groups. Our results are consistent with those reported[16c,23] in which GO or rGO could not completely cover the ITO surface with the spin-coating method because of their 2D nanosheet nature. Satisfactory device performance was obtained with thin rGO films as the p-contact for inverted PHJ perovskite solar cells, as we discuss in what follows.

Inverted PHJ perovskite solar cells were fabricated based on the device configuration ITO/GO (or rGO)/MAPbI$_3$ (330 nm)/ [6,6]-phenyl-C61-butyric acid methyl ester (PCBM, 70 nm)/Ag (100 nm), shown in **Figure 2**. A perovskite layer was deposited with a typical anti-solvent (AS) method[26] followed by a solvent-annealing (SA) treatment.[27] Chlorobenzene served as an antisolvent to introduce super-saturation to form the uniform perovskite film. Post-SA under N,N-dimethylformamide (DMF) vapor led to growth of PSK nanocrystals with enhanced grain size. Figure S4 (Supporting Information), shows top-view SEM images for all PSK films grown on ITO/GO or ITO/rGO substrates, for which pin-hole-free, close-packed and uniform perovskite crystals were produced for all devices. These perovskite nanocrystals have crystallinity confirmed with the X-ray powder diffraction (XRD) data shown in Figure S5 (Supporting Information). The side-view SEM images of the devices made of GO and other rGO as HEL are shown in Figure S6 (Supporting Information).

Figures 3a,b shows the photovoltaic performances and the corresponding efficiency of conversion of incident photons to current (IPCE) spectra, respectively, for the best cells made with varied GO and rGO as HEL; the photovoltaic parameters of the corresponding devices are summarized in **Table 1**. The inverted PHJ device made of PEDOT:PSS as HEL gave PCE 14.8%, which is similar to that reported elsewhere.[28] For the GO device, we obtained PCE 13.8%, which is much greater
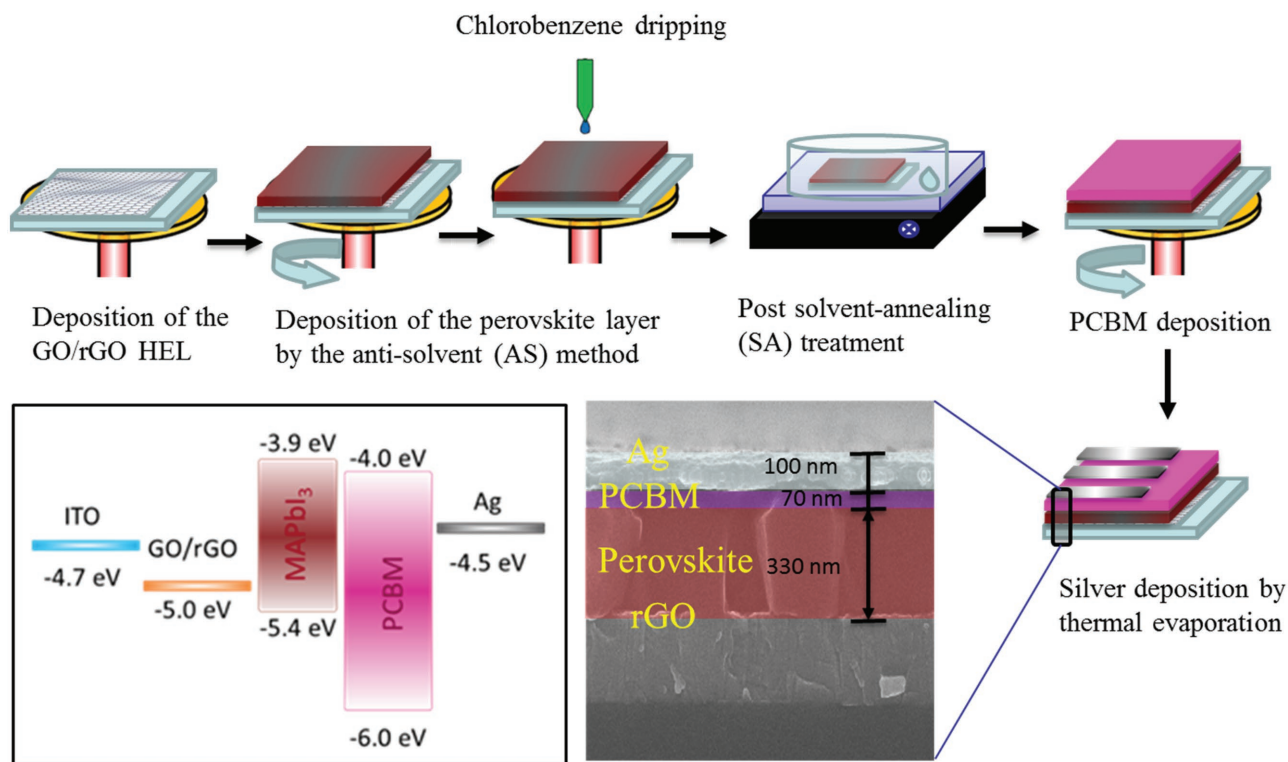
Figure 2. Device fabrication layer by layer for a perovskite layer produced with a combined antisolvent (AS) and solvent-annealing (SA) approach. The side-view SEM image shows the PHJ PSC device structure with each layer labeled in a separate color; the inset box shows a potential-energy level diagram for each component.

than that reported by Wu et al. (PCE = 12.4%).[15] All devices made of rGO as HEL showed greater photovoltaic performance (rGO-NH 16.0%, rGO-BH 15.3% and rGO-HBS 16.4%) than that of PEDOT:PSS and GO devices. The superior performances of rGO are due to their greater J_{SC} and V_{OC} values that outperform those of the reference devices, GO and PEDOT:PSS. Large currents for these rGO devices were confirmed with IPCE spectra shown in Figure 3b. The calculated J_{SC} values from these spectra are consistent with the J_{SC} values obtained from the J–V curves. All rGO devices show the IPCE spectral feature the same as that of the GO device but with IPCE values in the entire wavelength range greater than those of the GO device.

Regarding hysteresis, the PSC with an architecture consisting of a mesoporous TiO_2/perovskite/hole-extraction layer exhibited a large hysteresis according to the reverse and forward scan directions in the J–V measurements.[29] The reason for the occurrence of hysteresis in PSC is unclear.[30] A recent investigation[31] indicates that the dopants used in the HEL or EEL might significantly increase the hysteresis through extrinsic ion migration. In contrast, planar-structured PSC, especially with organic charge-extraction layers without added dopants, have been demonstrated to show a negligible hysteresis.[32] According to the results shown in Figure S7 (Supporting Information), only a slight hysteresis was observed for
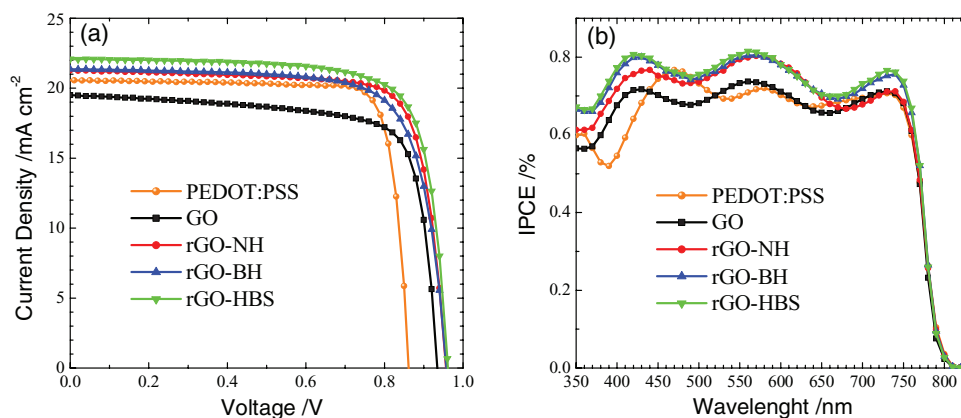
Figure 3. a) J–V curves and b) IPCE spectra of devices fabricated using HEL: PEDOT:PSS, GO, rGO-NH, rGO-BH, and rGO-HBS.

**ADVANCED
SCIENCE NEWS**

www.advancedsciencenews.com

**ADVANCED
ENERGY
MATERIALS**

www.advenergymat.de

Table 1. Photovoltaic parameters of inverted planar heterojunction perovskite solar cells fabricated with varied p-type HEL materials under simulated AM-1.5G illumination (power density 100 mW cm^{-2}).

Device[a]	J_{SC} [mA cm^{-2}]	V_{OC} [V]	FF	PCE[b] [%]
PEDOT:PSS	20.4	0.872	0.831	14.8 (13.3 ± 0.7)
GO	19.5	0.943	0.751	13.8 (12.1 ± 0.9)
rGO-NH	21.3	0.963	0.787	16.0 (14.5 ± 0.7)
rGO-BH	21.4	0.965	0.742	15.3 (13.5 ± 1.0)
rGO-HBS	22.1	0.962	0.770	16.4 (14.45 ± 0.9)

[a]The devices were fabricated with the following hole-extraction layers (HEL) under the same experimental conditions for all devices; [b]The average values shown in parentheses were obtained from 50 devices (35 devices for PEDOT:PSS) fabricated under the same experimental conditions.
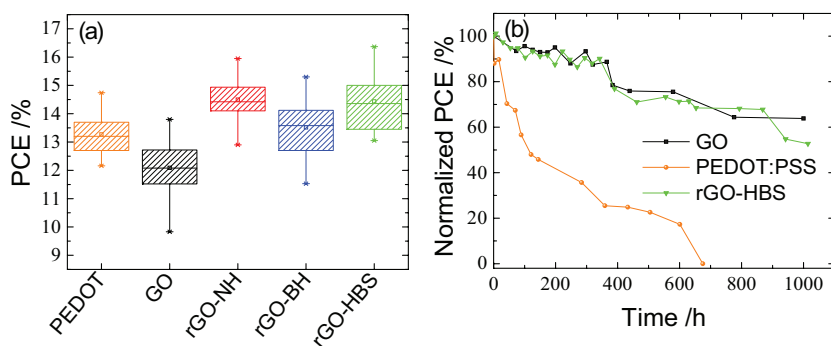
the rGO-BH-based perovskite solar cell; a negligible extent of hysteresis was observed for the GO, rGO-NH, and rGO-HBS devices. We speculate that the negligible hysteresis observed for our GO and rGO devices might be due to the thin HEL (≈2 nm, Figure S3, Supporting Information) in the absence of dopants so that no extrinsic ion migration occurred.

According to the device configuration shown in Figure 2, 50 devices were fabricated under the same experimental conditions for the GO and rGO-based devices of each type; the corresponding photovoltaic parameters are listed in Tables S2–S5 (Supporting Information); 35 identical PEDOT:PSS devices were fabricated for comparison, of which the results are shown in Table S6 (Supporting Information). **Figure 4**a compares the PCE distributions of these results with various hole-extraction layers, giving mean PCE/% 13.3 ± 0.7, 12.1 ± 0.9, 14.5 ± 0.7, 13.5 ± 1.0, and 14.45 ± 0.9 (shown in parenthesis in Table 1) for devices made with PEDO:PSS, GO, rGO-NH, rGO-BH and rGO-HBS, respectively; the corresponding box plots for J_{SC}, V_{OC}, and FF appear in Figure S8 (Supporting Information). The overall PV performances showed the order rGO-NH ≈ rGO-HBS > rGO-BH > PEDOT:PSS > GO. Each rGO device exhibited a device performance better than that of GO and PETDOT:PSS devices. The smaller average PCE and larger uncertainties of rGO-BH than of the other two rGO devices are attributed to a poor coverage of rGO-BH on the surface of

the ITO substrate. The rGO-NH devices showed the best mean PCE with the smallest standard deviation, indicating that the rGO-NH device has excellent stability and reproducibility in comparison with other devices.
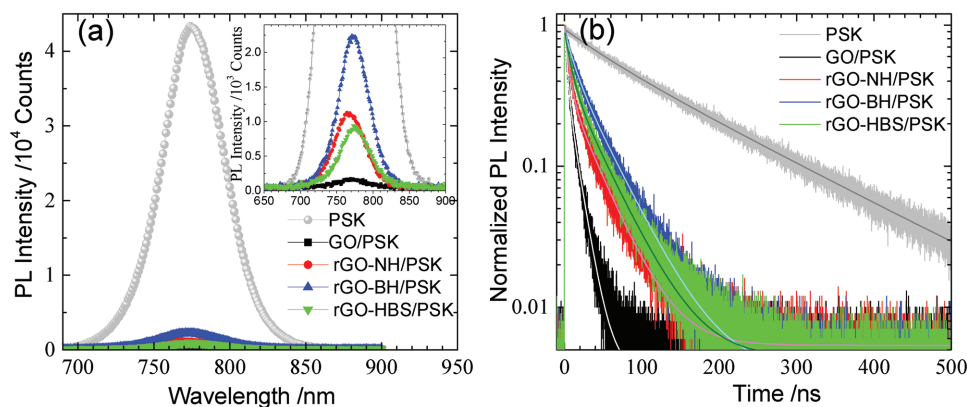
An important aspect for the commercialization of PSC is their enduring stability. The performances as a function of storage period for three devices, PEDOT:PSS, GO, and rGO-HBS, were measured for 1000 h at 25 °C and relative humidity 30% with no encapsulation; the results are illustrated in Figure 4b. The performance of the standard cell that was fabricated with PEDOT:PSS as the HEL degraded rapidly and became zero after 650 h, but the devices made of GO and rGO-HBS as HEL maintained half their initial efficiencies after storage for 1000 h, indicating the excellent long-term stability of the GO-based devices relative to an organic HEL material such as PEDOT:PSS.

The effect of surface coverage of rGO nanosheets on the ITO substrate was investigated for the rGO-NH devices on varying the concentration of hydrazine that acted as reducing agent to generate rGO-NH. As the XPS data show in Figure S9 (Supporting Information), and the analyzed data summarized in Table S7 (Supporting Information), when hydrazine at increased concentration was used to produce the rGO-NHH film, more oxygen-containing groups were removed and the rGO-NHH nanosheets became less hydrophilic. The poor coverage with agglomerated particles of rGO-NHH on the surface of ITO is indicated in the SEM images shown in Figure S9b (Supporting Information). This poor coverage causes a poor performance of the rGO-NHH device with a small fill factor and efficiency. Figure S9c (Supporting Information), shows the distribution of PCE and FF for one batch of the rGO-NHH and rGO-NH fabricated under the same experimental conditions; the PV performances of these rGO-NHH devices were much poorer than those of the rGO-NH devices because of the problem of surface coverage of the former devices. The formation of a uniform rGO film to cover more surface of ITO is hence an essential factor in optimization of the PV performance for the rGO devices. The film formation of the rGO nanosheets is related to the amount of hydrophilic groups on the surface; these groups can help to have a stable rGO suspension during spin-coating, but we have much reduction of rGO-HBS for which the film formation of rGO-HBS on ITO was not a problem. The SO$_3$H groups remaining on the surface might help to produce a stable rGO suspension and to avoid agglomeration of rGO to form a uniform HEL film for the superior device performance observed herein. With careful control of the amount of reducing agent to form the uniform rGO films on ITO, both rGO-HBS and rGO-NH devices attained PCE exceeding 16%, which is much greater than that reported by Yeo et al.[17]

To investigate the hole selectivity of the perovskite layer to the ITO anode, we measured steady-state PL spectra and transient PL decays with the time-correlated single-photon counting (TCSPC) technique. Bilayer samples were prepared with a perovskite layer deposited on either an ITO/GO or

Figure 4. a) Statistical boxplots of device performance for PHJ PSC devices made of varied HEL with 50 devices fabricated under the same experimental conditions for cells of each type. b) Profiles of efficiency stability of the PHJ devices with HEL made of PEDOT:PSS, GO, and rGO-HBS as a function of storage period.

**ADVANCED
SCIENCE NEWS**
www.advancedsciencenews.com

**ADVANCED
ENERGY
MATERIALS**
www.advenergymat.de

Figure 5. a) Photoluminescence (PL) spectra and b) transient PL decay profiles of PSK on ITO and on varied HEL, GO, rGO-NH, rGO-BH, and rGO-HBS as indicated.
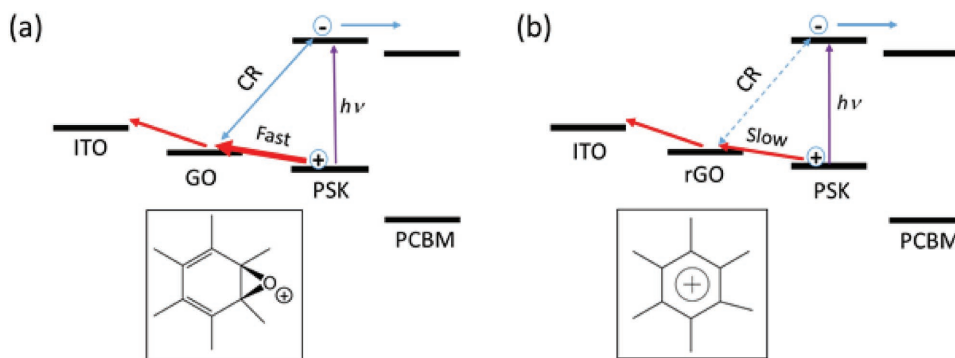
an ITO/rGO substrate; the reference sample is only the perovskite deposited on the ITO substrate. Relative to the PSK only sample, a significant quenching of PL intensities was observed, in **Figure 5**a, for the bilayer samples with the perovskite layer in contact with either the GO or rGO HEL, but, as shown in the inset of Figure 5a, the effect of PL quenching is more pronounced for GO than for other rGO layers; the PL intensities show an order ITO/PSK > ITO/rGO-BH/PSK > ITO/rGO-NH/PSK ~ ITO/rGO-HBS/PSK > ITO/GO/ PSK. This result indicates that GO has a hole-extraction characteristic better than the other rGO layers to quench the PL intensity effectively. The PL intensities are regarded as indirect markers for the lifetimes of the excitons produced in these samples, but direct evidence arose from measurements of the PL decay kinetics of these samples with the TCSPC technique.

The normalized transient PL decays of the corresponding samples (λ_{ex} = 635 nm and λ_{PL} = 770 nm) are shown in Figure 5b, which exhibit the trend of decay feature the same as the trend of PL quenching. All PL transients were fitted with a bi-exponential decay function; the corresponding lifetimes and relative amplitudes are summarized in Table S8 (Supporting Information). We assign the first decay component corresponding to the nonradiative relaxation of the surface state in the grain boundaries of the perovskite and the second decay component to the radiative recombination or nonradiative relaxation in the bulk.[33] For the pristine thin-film perovskite on the ITO substrate, the first and the second decay coefficients were 54 ns and 153 ns, respectively, but both decay coefficients became significantly decreased when a PSK layer was in contact with HEL of GO, rGO-NH, rGO-BH, and rGO-HBS because of efficient hole transfer from PSK to HEL. The trend of average PL lifetimes (τ_{PL}) of the samples shows the order ITO/PSK > ITO/rGO-BH/PSK > ITO/rGO-HBS/PSK > ITO/ rGO-NH/PSK > ITO/GO/PSK. Assuming that all PL quenches are due to the effect of hole extraction, we can evaluate the hole extraction times (τ_h) (Table S8, Supporting Information) to show the ability of hole extraction; the trend of hole extraction rate coefficients ($1/\tau_h$) shows the order GO > rGO-NH > rGO-HBS > rGO-BH, indicating that GO is the most efficient HEL compared to all rGO. As the photovoltaic results show in Figures 3 and 4, the GO device exhibited the worst PV performance compared to all rGO devices. We must therefore understand how

the most rapid hole extraction of GO produces the poorest performance compared to those of the rGO devices.

We first assume that hole extraction occurs rapidly in GO because of oxygen-containing functional groups that donate electronic density to the hole of the excited perovskite (so that the hole in PSK is extracted into the HEL) more rapidly than hole extraction directly from the benzene rings on the surface of GO. If those oxygen groups become reduced, the hole extraction from PSK to HEL would be slowed. We therefore designed a control experiment to reduce those oxygen-containing functional groups on applying hydrazine vapor to the GO film at temperatures 50 and 100 °C. As the XPS data show in Figure S10 and Table S9 (Supporting Information), the oxygen-containing functional groups and the trap states on the GO surface were significantly diminished upon reduction with N_2H_4 vapor;[16a,34] the content of C=C double bonds increased systematically from 39% (GO) to 64% (rGO-NH-50 °C) and further to 73% (rGO-NH-100 °C) in those rGO. As transient PL decays show in Figure S11 (Supporting Information) (fitted decay coefficients for each sample are summarized in Table S10 of the Supporting Information), we confirmed that, on increasing the extent of GO reduction, both PL intensities and hole-extraction times became enhanced, which proves our hypothesis that the efficient hole extraction in GO arises from the oxygen-containing functional groups. When those oxygen groups were reduced, hole injection into the C=C double bonds on the global rGO surface became much slowed, as we observed.

Although we have proved that the oxygen-containing functional groups on GO surface act as the hole-extraction sites so that GO can quench PL efficiently, the photocurrents and fill factors of the GO devices are less than those of the rGO devices (Figure S8, Supporting Information). More rapid hole injection of GO hence renders device performance worse than those of the rGO devices showing smaller rates of hole injection. This anomalous behavior might be explained in a schematic picture shown in **Scheme 2**. These oxygen-containing groups attached to the tetrahedrally coordinated carbon atoms ($-C_{sp3}-O-C_{sp3}-$, $-C_{sp3}-OH$, $-C_{sp3}-COOH$, etc.) can extract holes from the perovskite efficiently but also generate these holes localized on the oxygen atoms (one example is shown in Scheme 2a), so that the subsequent hole transfer to the ITO

ADVANCED
SCIENCE NEWS
www.advancedsciencenews.com

ADVANCED
ENERGY
MATERIALS
www.advenergymat.de

Scheme 2. Schematic illustration of a mechanism of charge transfer for a) GO and b) rGO to rationalize the observed hole-extraction kinetics at the HEL/PSK interface and the corresponding photovoltaic performance between the GO and the rGO devices. The box insets shown in (a) and (b) represent the localized holes in the oxygen atom and the delocalized hole in the benzene ring for the cases of GO and rGO, respectively. The CR represents charge recombination in the GO (rGO)/PSK interface.

substrate becomes a bottleneck. The localized holes on oxygen atoms might also enhance the possibility of charge recombination (CR) to occur at the GO/PSK interface. In contrast, if those oxygen-containing groups become reduced, the hole injection from PSK to HEL occurs most likely at the C=C double bonds of the benzene rings in rGO, as illustrated in Scheme 2b. Even though this hole-extraction is slower than that occurring on an oxygen-containing group in GO, it generates delocalized holes (Scheme 2b) that are in resonance in the π-conjugation system of the graphene structure. The delocalized holes thereby transferred easily to the ITO substrate; the CR at the rGO/PSK interface became minimized. For this reason the rGO devices show a PV performance greater than that of the GO devices. The mechanism shown in Scheme 2 thus rationalizes what we have observed as the anomalous behavior in relation to the photovoltaic performance with respect to the rate of hole extraction for the HEL between GO and rGO.

To prove the proposed mechanism shown in Scheme 2, we conducted transient photoelectric measurements under five bias light intensities for both GO and rGO-HBS devices using a technique reported elsewhere.[35] For the transient photocurrent decays measured under short-circuit conditions, we observed rapid transient decays for both GO and rGO-HBS devices independent of the bias light intensities (Figures S12a and 12b, Supporting Information). This capacitive behavior is typical for a p–i–n photodiode,[36] for which charge accumulation in the HEL/PSK interface becomes a bottleneck to be observed. The photocurrent transients hence invariably gave a decay coefficient ≈300 ns, which is equal to the RC time constants of the devices. Charge collection times of both devices are hence RC-limited and the duration of hole propagation from GO or rGO to the ITO substrate should be the observed ≈300 ns, which is much larger than the charge-extraction durations obtained from the PL decay measurements (Figure 5b and Table S8, Supporting Information). In contrast, for the transient photovoltage decays measured under open-circuit conditions, the charge recombination times can be well resolved as the raw data shown in Figures S13a and 13b (Supporting Information), for GO and rGO-HBS, respectively. All photovoltage decay profiles were fitted with a single-exponential decay function with values of CR decay coefficient (τ_{rec}) shown in **Figure 6**. Our
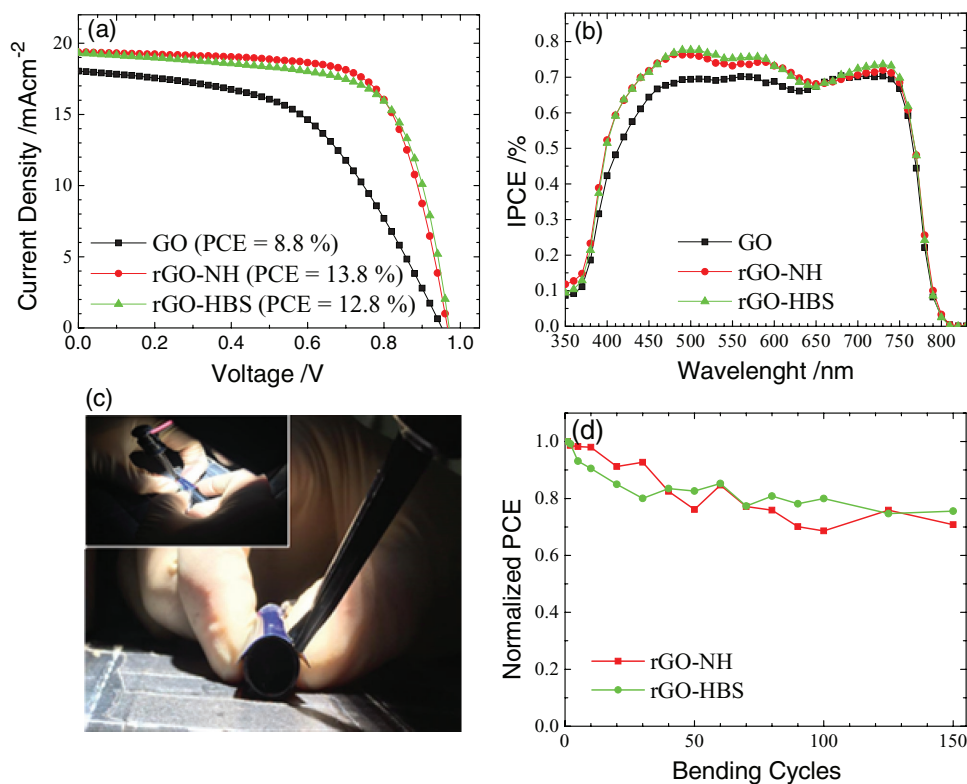
results clearly indicate that the CR times are much greater for the rGO-HBS device than for the GO device, consolidating our mechanism illustrated in Scheme 2.

Based on both PL decay and transient photoelectric measurements, we conclude that a rapid charge extraction in the GO device also led to the occurrence of a rapid charge recombination because the hole propagation from the HEL to the ITO substrate would become a bottleneck to overcome. As a result, the efficiencies of charge collection in the rGO devices were greater than in the GO device, resulting in larger J_{SC} (as reflected from the IPCE spectra shown in Figure 3b) and overall better performance for the former than the latter devices.

Processing of rGO at a temperature less than 150 °C allowed us to fabricate high-performance flexible PHJ perovskite devices using rGO as HEL. We therefore replaced the rigid ITO/glass substrate with a flexible ITO/PEN substrate with the same device fabrication shown in Figure 2. The current–voltage curves and IPCE action spectra of such flexible devices with GO, rGO-NH, and rGO-HBS as HEL are shown in **Figure 7**a,b, respectively. The device performances show an order rGO-NH > rGO-HBS > GO with the best cell made of rGO-NH attaining PCE 13.8%. These flexible rGO devices show performance
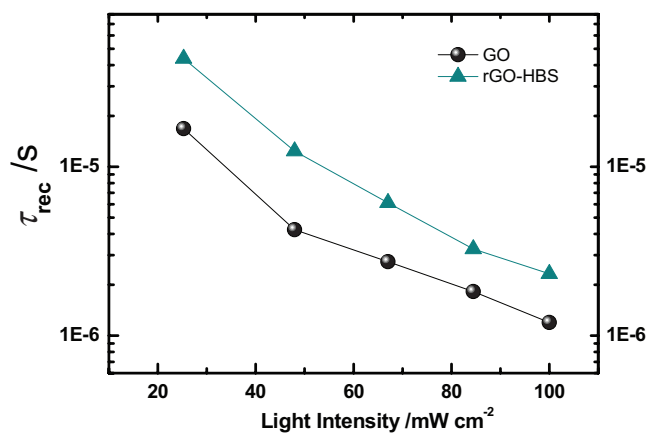
Figure 6. Charge recombination time coefficient (τ_{rec}) determined at five bias light intensities for the GO and the rGO-HBS devices as indicated.

**ADVANCED
SCIENCE NEWS**

www.advancedsciencenews.com

**ADVANCED
ENERGY
MATERIALS**

www.advenergymat.de

Figure 7. a) Current–voltage curves and b) IPCE action spectra of flexible devices made of GO, rGO-NH, and rGO-HBS as HEL. c) The bending experiments were performed with the flexible devices bent to a tube of radius 5 mm, d) the normalized PCE of flexible devices as a function of bending cycles are shown.

poorer than that of their rigid ITO/glass analogues because of greater sheet resistance and smaller transmittance of the ITO/PEN substrate at visible spectral region. For flexible devices, the mechanical flexibility and durability under a bending stress are important characteristics to be considered; they were tested accordingly. For the bending test, we manually bent the device (Figure 7c) and measured the J–V curve under the flat and bent conditions. Photovoltaic properties were evaluated under both flat and bent conditions for the first three cycles; the PV results are listed in Table S11 (Supporting Information). Only a slight PCE degradation was observed when the device was measured in a bent conformation. Figure 7d shows that the device maintained up to 70% of its initial performance after mechanical bending up to 150 cycles.

3. Conclusion

Solution-processed GO and rGO nanosheets of various types were synthesized and deposited on ITO substrate as a hole-extraction layer for high-performance inverted PHJ PSC. The rGO samples were prepared with three reducing agents—hydrazine, sodium borohydride and 4-hydrazino benzenesulfonic acid—to produce three rGO labeled as rGO-NH, rGO-BH and rGO-HBS, respectively. All three rGO-based devices showed PCE superior to that of the GO device (PCE 13.8%) and that of the PEDOT:PSS device (PCE 14.8%) with the best cells of the rGO-NH and rGO-HBS devices attaining PCE 16.0% and

16.4%, respectively, with excellent stability and reproducibility. The robust flexible device based on rGO-NH was fabricated to show PCE 13.8% and maintained 70% of its initial performance after 150 bending cycles. PL and transient PL decays were investigated to show the rates of hole extraction with the order GO > rGO-NH > rGO-HBS > rGO-BH, which is contrary to the photovoltaic results that show the poorest performance for the GO device. Controlled reduction experiments confirmed that the hole-extraction times were significantly enhanced when the oxygen-containing groups were largely reduced. Transient photovoltage decay measurements showed that the charge recombination times of the rGO-HBS device are much greater than those of the GO device. These results indicate that the localized holes on oxygen atoms were produced rapidly but the transfer of the localized holes into the ITO surface could become a bottleneck for rapid charge recombination to occur at the PSK/GO interface. In contrast, when those oxygen-containing groups were reduced in rGO, slower hole injection from PSK to rGO might occur in the global graphene structure, but delocalized holes in the benzene rings would retard charge recombination to improve the performances of the rGO devices relative to the GO device. Our results showed also that the control of the extent of reduction to produce uniform rGO films with superior surface coverage on the ITO substrate is an important factor to improve the device performance. Work is in progress to improve the surface coverage of rGO on ITO and to increase the rate of hole injection by functionalization of the rGO surface for further enhanced device performance.

ADVANCED
SCIENCE NEWS
www.advancedsciencenews.com

ADVANCED
ENERGY
MATERIALS
www.advenergymat.de

4. Experimental Section

Synthesis and Device Fabrication: An experimental scheme to synthesize graphene oxide in DMF solution according to Hummers method[20] is shown in Figure S1 (Supporting Information); the AFM image of GO deposited on Si wafer shows GO and rGO to have thickness ≈1 nm (Figure S2, Supporting Information). For reduction of GO with hydrazine (rGO-NH), hydrazine (5 µL) was added a solution of GO (100 mL, 0.3 mg mL^{-1} in DMF) and refluxed for 14 h at 80–85 °C. The resulting black solution was centrifuged and washed with DMF several times. For reduction of GO by NaBH$_4$ (rGO-BH), solution of NaBH$_4$ (5 mL, 10 mg mL^{-1}) was added to an aqueous solution of GO (20 mL, 0.4 mg mL^{-1}); the solution was stirred at 80 °C for 3 h; the resulting black solution was centrifuged and washed several times with water and then DMF before transfer to DMF (0.5 mg mL^{-1}). For reduction of GO with HBS, HBS (500 mg) was added to GO aqueous solution (15 mL, 0.5 mg mL^{-1}) and stirred at 60 °C for 5 h before filtration and washing several times with water and DMF and transfer to DMF. For all rGO solutions, the concentration was 0.5 mg mL^{-1}. For investigation of the reduction level of rGO-NH on the effect of the device performance, two amounts of hydrazine were used. For a small extent of reduction, the same amount of rGO-NH was used; ten times the amount of hydrazine (50 µL) was used for reduction of GO at the increased level of reduction, which was defined as rGO-NHH. For controlled experiments on GO reduction in photoluminescence analysis, hydrazine vapor served as reducing agent; ITO/GO samples were exposed to hydrazine vapor at temperatures 50 and 100 °C for 12 h.

CH$_3$NH$_3$I (MAI) was synthesized as reported elsewhere.[37] To prepare the perovskite precursor solution, MAI and PbI$_2$ (molar ratio 1:1) powders were mixed in anhydrous DMF with concentration 40 mass%. The solution was stirred for at least 4 h at 70 °C and filtered through a polyvinylidene difluoride (PVDF) membrane (0.45 µm) before device fabrication. The devices were fabricated with a p–i–n configuration ITO/rGO (GO) /CH$_3$NH$_3$PbI$_3$/PCBM/Ag. The etched ITO substrates were cleaned and exposed to ultraviolet light and O$_3$ for 18 min. rGO and GO solutions (0.5 mg mL^{-1} in DMF) were spin-coated onto the substrates at 3500 rpm for 40 s. After baking at 120 °C for 15 min, the substrates were transferred into a glove box for subsequent depositions of perovskite and electrode. The perovskite precursor solution was dripped onto the ITO/rGO (GO) substrate spinning at rate 5000 rpm. The total period of the spin coating was 15 s, chlorobenzene serving as an antisolvent was injected onto the substrate after spinning for 5 s. The substrates were then annealed at 100 °C for 2 min; the samples were treated to SA under DMF vapor for 10 min at the same temperature. Afterward, PCBM (20 mg, FEM Tech.) was dissolved in chlorobenzene (1 mL) and spin-coated on top of the perovskite layer at 1000 rpm for 30 s. The silver back-contact electrode (100 nm) was eventually deposited via thermal evaporation in a vacuum chamber.

Characterization of Materials and Devices: The current–voltage characteristics were measured with a digital source meter (Keithley 2400) with the device under one-sun illumination (AM 1.5G, 100 mW cm^{-2}) from a solar simulator (XES-40S1, SAN-E1). The spectra of the IPCE of the corresponding devices were recorded with a system consisting of a Xe lamp (PTiA-1010, 150W), a monochromator (PTi, 1200 g mm^{-1} blazed at 500 nm) and a source meter (Keithley 2400). XRD patterns were recorded with an X-ray diffractometer (BRUKER AXS, D8 Advance, Cu Kα, λ = 1.5418 Å). SEM were acquired with a microscope (Hitachi SU-8010) to determine the morphology of the films. Absorption spectra were measured with a spectrophotometer (JASCO V-570); the sample was excited with a He–Ne laser and emission was collected at 45° with a lens; the PL emission was measured at 770 nm for all samples under similar excitation conditions. We mapped the entire film on translating the sample stage in steps of sub-mm resolution. XPS were recorded with samples prepared on silicon wafer substrates at beamline 24A in Taiwan Light Source of National Synchrotron Radiation Research Center (NSRRC). For XPS, X-radiation with photon energy 700 eV was used; the binding energies were calibrated against the bulk Au 4f7/2 core level (84.00 eV). Infrared spectra were recorded with an interferometric

spectrometer (JASCO-FT/IR-6100) in transmittance mode; the resolution of the instrument was set at 4 cm^{-1} during the measurements. Thin films of GO and rGO were prepared with thermal annealing (70 °C) of precursor solutions drop-cast onto a BaF$_2$ substrate. Raman spectral measurements of GO and rGO films dispersed in water were measured on exciting the samples (wavelength 632.8 nm, He–Ne laser) using a laboratory-built confocal Raman microspectrometric system; the laser power at the sample position was set to a few milliwatts; exposure duration was 60 s.[38]

Supporting Information

Supporting Information is available from the Wiley Online Library or from the author.

Conflict of Interest

The authors declare no conflict of interest.

[1] a) M. Saliba, T. Matsui, K. Domanski, J.-Y. Seo, A. Ummadisingu, S. M. Zakeeruddin, J.-P. Correa-Baena, W. R. Tress, A. Abate, A. Hagfeldt, M. Grätzel, *Science* **2016**, *354*, 206; b) D. Bi, C. Yi, J. Luo, J.-D. Décoppet, F. Zhang, S. M. Zakeeruddin, X. Li, A. Hagfeldt, M. Grätzel, *Nat. Energy* **2016**, *1*, 16142.

[2] a) S. Kazim, M. K. Nazeeruddin, M. Grätzel, S. Ahmad, *Angew. Chem. Int. Ed.* **2014**, *53*, 2812; b) Y.-C. Hsiao, T. Wu, M. Li, Q. Liu, W. Qin, B. Hu, *J. Mater. Chem. A* **2015**, *3*, 15372; c) T. Salim, S. Sun, Y. Abe, A. Krishna, A. C. Grimsdale, Y. M. Lam, *J. Mater. Chem. A* **2015**, *3*, 8943.

[3] T. Liu, K. Chen, Q. Hu, R. Zhu, Q. Gong, *Adv. Energy Mater.* **2016**, *6*, 1600457.

[4] a) X. Yin, P. Chen, M. Que, Y. Xing, W. Que, C. Niu, J. Shao, *ACS Nano* **2016**, *10*, 3630; b) H. Zhang, J. Cheng, F. Lin, H. He, J. Mao, K. S. Wong, A. K. Y. Jen, W. C. H. Choy, *ACS Nano* **2016**, *10*, 1503.

[5] M. Ye, X. Hong, F. Zhang, X. Liu, *J. Mater. Chem. A* **2016**, *4*, 6755.

[6] a) M.-H. Li, P.-S. Shen, K.-C. Wang, T.-F. Guo, P. Chen, *J. Mater. Chem. A* **2015**, *3*, 9011; b) L. Meng, J. You, T.-F. Guo, Y. Yang, *Acc. Chem. Res.* **2016**, *49*, 155.

[7] H. Kim, K.-G. Lim, T.-W. Lee, *Energy Environ. Sci.* **2016**, *9*, 12.

[8] P. Dhingra, P. Singh, P. J. S. Rana, A. Garg, P. Kar, *Energy Technol.* **2016**, *4*, 891.

[9] J. H. Heo, H. J. Han, D. Kim, T. K. Ahn, S. H. Im, *Energy Environ. Sci.* **2015**, *8*, 1602.

**ADVANCED
SCIENCE NEWS**

www.advancedsciencenews.com

**ADVANCED
ENERGY
MATERIALS**

www.advenergymat.de

[10] a) W.-Y. Chen, L.-L. Deng, S.-M. Dai, X. Wang, C.-B. Tian, X.-X. Zhan, S.-Y. Xie, R.-B. Huang, L.-S. Zheng, *J. Mater. Chem. A* **2015**, *3*, 19353; b) J. You, L. Meng, T.-B. Song, T.-F. Guo, Y. Yang, W.-H. Chang, Z. Hong, H. Chen, H. Zhou, Q. Chen, Y. Liu, N. De Marco, Y. Yang, *Nat. Nano* **2016**, *11*, 75.

[11] S. Seo, I. J. Park, M. Kim, S. Lee, C. Bae, H. S. Jung, N.-G. Park, J. Y. Kim, H. Shin, *Nanoscale* **2016**, *8*, 11403.

[12] X. Bao, Q. Zhu, T. Wang, J. Guo, C. Yang, D. Yu, N. Wang, W. Chen, R. Yang, *ACS Appl. Mater. Interfaces* **2015**, *7*, 7613.

[13] H. Sung, N. Ahn, M. S. Jang, J.-K. Lee, H. Yoon, N.-G. Park, M. Choi, *Adv. Energy Mater.* **2016**, *6*, 1501873.

[14] a) G. A. Sepalage, S. Meyer, A. Pascoe, A. D. Scully, F. Huang, U. Bach, Y.-B. Cheng, L. Spiccia, *Adv. Energy Mater.* **2015**, *25*, 5650; b) S. Ye, W. Sun, Y. Li, W. Yan, H. Peng, Z. Bian, Z. Liu, C. Huang, *Nano Lett.* **2015**, *15*, 3723.

[15] a) Z. Wu, S. Bai, J. Xiang, Z. Yuan, Y. Yang, W. Cui, X. Gao, Z. Liu, Y. Jin, B. Sun, *Nanoscale* **2014**, *6*, 10505; b) C.-C. Chung, S. Narra, E. Jokar, H.-P. Wu, E. W.-G. Diau, *J. Mater. Chem. A* **2017**, *5*, 13957.

[16] a) I. Jung, D. A. Dikin, R. D. Piner, R. S. Ruoff, *Nano Lett.* **2008**, *8*, 4283; b) G. Eda, C. Mattevi, H. Yamaguchi, H. Kim, M. Chhowalla, *J. Phys. Chem. C* **2009**, *113*, 15768; c) S.-S. Li, K.-H. Tu, C.-C. Lin, C.-W. Chen, M. Chhowalla, *ACS Nano* **2010**, *4*, 3169.

[17] J.-S. Yeo, R. Kang, S. Lee, Y.-J. Jeon, N. Myoung, C.-L. Lee, D.-Y. Kim, J.-M. Yun, Y.-H. Seo, S.-S. Kim, S.-I. Na, *Nano Energy* **2015**, *12*, 96.

[18] a) C. K. Chua, M. Pumera, *Chem. Soc. Rev.* **2014**, *43*, 291; b) S. Pei, H.-M. Cheng, *Carbon* **2012**, *50*, 3210.

[19] D.-Y. Lee, S.-I. Na, S.-S. Kim, *Nanoscale* **2016**, *8*, 1513.

[20] A. E. Shalan, T. Oshikiri, S. Narra, M. M. Elshanawany, K. Ueno, H.-P. Wu, K. Nakamura, X. Shi, E. W.-G. Diau, H. Misawa, *ACS Appl. Mater. Interfaces* **2016**, *8*, 33592.

[21] Y. Shen, P. Zhou, Q. Q. Sun, L. Wan, J. Li, L. Y. Chen, D. W. Zhang, X. B. Wang, *Appl. Phys. Lett.* **2011**, *99*, 14191.

[22] Y. Xu, H. Bai, G. Lu, C. Li, G. Shi, *J. Am. Chem. Soc.* **2008**, *130*, 5856.

[23] a) J.-M. Yun, J.-S. Yeo, J. Kim, H.-G. Jeong, D.-Y. Kim, Y.-J. Noh, S.-S. Kim, B.-C. Ku, S.-I. Na, *Adv. Mater.* **2011**, *23*, 4923; b) J. Liu, M. Durstock, L. Dai, *Energy Environ. Sci.* **2014**, *7*, 1297.

[24] S.-J. Qiao, X.-N. Xu, Y. Qiu, H.-C. Xiao, Y.-F. Zhu, *Nanomaterials* **2016**, *6*, 29.

[25] R. S. Hidalgo, D. López-Díaz, M. M. Velázquez, *Langmuir* **2015**, *31*, 2697.

[26] M. Xiao, F. Huang, W. Huang, Y. Dkhissi, Y. Zhu, J. Etheridge, A. Gray-Weale, U. Bach, Y.-B. Cheng, L. Spiccia, *Angew. Chem., Int. Ed. Engl.* **2014**, *126*, 10056.

[27] Z. Xiao, Q. Dong, C. Bi, Y. Shao, Y. Yuan, J. Huang, *J. Adv. Mater.* **2014**, *26*, 6503.

[28] J. Liu, S. Pathak, T. Stergiopoulos, T. Leijtens, K. Wojciechowski, S. Schumann, N. Kausch-Busies, H. J. Snaith, *J. Phys. Chem. Lett.* **2015**, *6*, 1666.

[29] a) C. Huang, C. Liu, Y. Di, W. Li, F. Liu, L. Jiang, J. Li, X. Hao, H. Huang, *ACS Appl. Mater. Interfaces* **2016**, *8*, 8520; b) H.-S. Kim, N.-G. Park, *J. Phys. Chem. Lett.* **2014**, *5*, 2927.

[30] a) C. Li, A. Guerrero, Y. Zhong, S. Huettner, *J. Phys.: Condens. Matter* **2017**, *29*, 193001; b) H. J. Snaith, A. Abate, J. M. Ball, G. E. Eperon, T. Leijtens, N. K. Noel, S. D. Stranks, J. T.-W. Wang, K. Wojciechowski, W. Zhang, *J. Phys. Chem. Lett.* **2014**, *5*, 1511; c) H.-S. Kim, I.-H. Jang, N. Ahn, M. Choi, A. Guerrero, J. Bisquert, N.-G. Park, *J. Phys. Chem. Lett.* **2015**, *6*, 4633.

[31] Z. Li, C. Xiao, Y. Yang, S. P. Harvey, D. H. Kim, J. A. Christians, M. Yang, P. Schulz, S. U. Nanayakkara, C.-S. Jiang, J. M. Luther, J. J. Berry, M. C. Beard, M. M. Al-Jassim, K. Zhu, *Energy Environ. Sci.* **2017**, *10*, 1234.

[32] C.-H. Chiang, C.-G. Wu, *Nat. Photonics* **2016**, *10*, 196.

[33] a) D. Shi, V. Adinolfi, R. Comin, M. Yuan, E. Alarousu, A. Buin, Y. Chen, S. Hoogland, A. Rothenberger, K. Katsiev, Y. Losovyj, X. Zhang, P. A. Dowben, O. F. Mohammed, E. H. Sargent, O. M. Bakr, *Science* **2015**, *347*, 519; b) W. Nie, H. Tsai, R. Asadpour, J.-C. Blancon, A. J. Neukirch, G. Gupta, J. J. Crochet, M. Chhowalla, S. Tretiak, M. A. Alam, H.-L. Wang, A. D. Mohite, *Science* **2015**, *347*, 522.

[34] S. Kaniyankandy, S. N. Achary, S. Rawalekar, H. N. Ghosh, *J. Phys. Chem. C* **2011**, *115*, 19110.

[35] L.-L. Li, Y.-C. Chang, H.-P. Wu, E. W.-G. Diau, *Int. Rev. Phys. Chem.* **2012**, *31*, 420.

[36] B. E. A. Saleh, M. C. Teich, *Fundamentals of Photonics*, 2nd ed., John Wiley & Sons, Inc., Hoboken, NJ **2007**, p. 758.

[37] K.-C. Wang, J.-Y. Jeng, P.-S. Shen, Y.-C. Chang, E. W.-G. Diau, C.-H. Tsai, T.-Y. Chao, H.-C. Hsu, P.-Y. Lin, P. Chen, T.-F. Guo, T.-C. Wen, *Sci. Rep.* **2014**, *4*, 4756.

[38] H. N. Noothalapati Venkata, N. Nomura, S. Shigeto, *J. Raman Spectrosc.* **2011**, *42*, 1913.